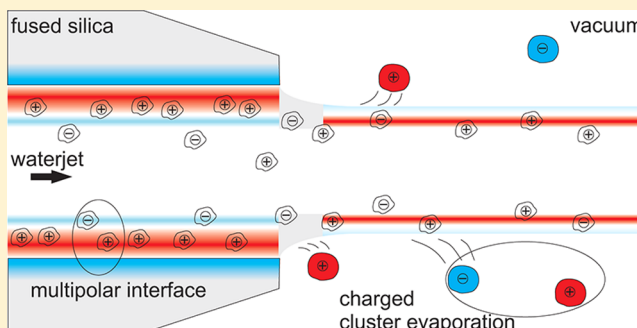


Electrokinetic Charging and Evidence for Charge Evaporation in Liquid Microjets of Aqueous Salt Solution

Natalie Preissler, Franziska Buchner, Thomas Schultz, and Andrea Lübcke*

Max-Born-Institut für nichtlineare Optik und Kurzzeitspektroskopie, Max-Born-Strasse 2A, 12489 Berlin, Germany

ABSTRACT: Electrokinetic charging of aqueous microjets was characterized by measuring streaming currents as a function of sodium iodide salt concentration. Measured streaming currents at high salt concentrations (up to 0.5 M) varied nonmonotonically with the jet velocity and can be explained by a multipolar charge distribution at the nozzle–water interface. In the case of potassium fluoride no multipolar charge distribution is observed. Electrokinetic potentials were estimated from the streaming currents, under the assumption that all excess charges are confined within the liquid jet. Measured photoelectron spectra indicate much smaller streaming potentials. To resolve the apparent discrepancy, we propose that a significant fraction of excess charges evaporates in the form of ion–water clusters.



INTRODUCTION

Thin liquid jets with diameters in the range of a few micrometers allow the investigation of liquid matter with traditional gas-phase spectroscopic techniques. One particular application is photoelectron spectroscopy, both static and time-resolved, which allows the direct characterization of electron binding energies in solvents and solutes. Interfacial effects at the liquid–vacuum interface are one exciting aspect that can be probed in such experiments. Recent examples for such work include the direct experimental observation of surface propensities for a variety of ions.^{1–4}

In this paper, we consider the effect of electrokinetic charging in liquid jet photoelectron spectroscopy. Electrokinetic charging creates a potential difference between the liquid jet and the electron spectrometer and therefore electrostatically accelerates or retards emitted photoelectrons. A number of recent photoelectron studies rely on elevated salt concentrations to suppress electrokinetic charging in water jets,^{1–8} but there exists no systematic investigation of electrokinetic charging in the presence of different salt concentrations.

Electrokinetic charging occurs when a solvent containing ions flows over a surface and carries one type of ions away while the counterions remain bound at the static interface. In the experimental setup considered here, the liquid flows through a fused-silica nozzle into a vacuum chamber. A schematic of the electrokinetic charging mechanism at the exit of a fused silica nozzle is depicted in Figure 1. Such fused silica nozzles are used in our and in numerous other liquid jet experiments.^{1–10} In contact with water, a silica surface becomes hydrated and forms a Haber–Haugaard layer containing acidic hydroxyl (–OH) groups.^{11,12} The acidity of hydroxyl groups will lead to a negative surface charge at neutral pH.¹³ Charging of the glass surface relative to the solution creates an electrostatic potential and leads to the formation of a diffusely bound Gouy–

Chapman layer of counterions. The amount of negative excess surface charge depends on the ion concentration in the solution. The higher the ion concentration, the more excess charge can be accumulated. The ion concentration in the diffuse Gouy–Chapman layer falls off exponentially with increasing distance from the surface. The Debye length r_D denotes the characteristic distance over which the potential drops to e^{-1} relative to the surface potential¹⁴

$$r_D = \sqrt{\frac{\epsilon_0 \epsilon_r^j kT}{2e^2 N_A S}} \quad (1)$$

where e is the elementary charge, N_A is Avogadro's constant, ϵ_0 is the vacuum permittivity, ϵ_r^j is the relative permittivity of the jet, k is Boltzmann's constant, T is the jet temperature, and S is the ionic strength. The ionic strength depends on the ionic charge z and the concentration c of all ions in the solution:

$$S = \frac{1}{n} \sum_{i=1}^n c_i z_i^2 \quad (2)$$

For $T = 298$ K and with water as the solvent ($\epsilon_r^j = 78.54$), the Debye length is given as

$$r_D = 3.04 \times 10^{-10} \frac{1}{\sqrt{S}} m \sqrt{\text{mol/L}} \quad (3)$$

If the solution flows through the nozzle, part of the diffusely bound ions are carried away, leading to electrokinetic charging by a net separation of charges.

Received: May 16, 2012

Revised: January 9, 2013

Published: January 21, 2013



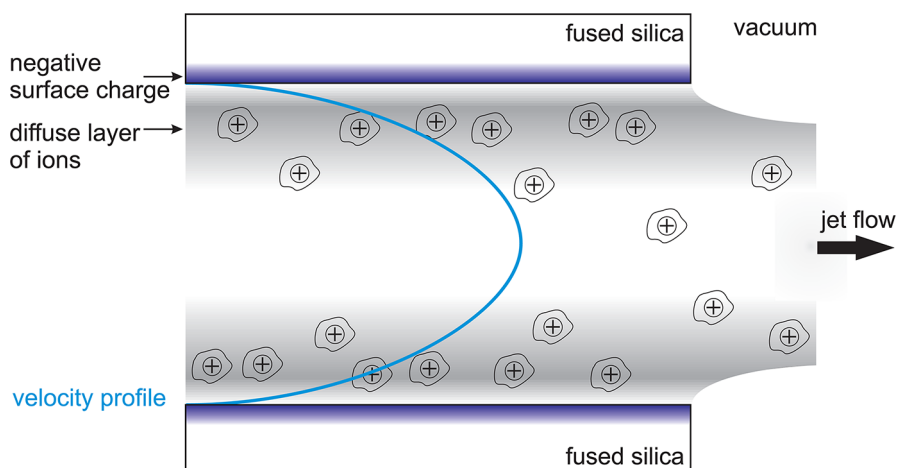


Figure 1. Schematic depiction of the cross section of a liquid jet flowing through a fused silica nozzle into vacuum. Hydration of the silica surface leads to negative excess surface charge (blue), which, in turn, leads to formation of a diffuse Gouy–Chapman layer of cations (gray). Due to the nonuniform velocity profile of the liquid inside the nozzle, ions in the diffuse layer are sheared off and cause significant charging of the liquid jet.

For laminar flow, the velocity profile is parabolic; the velocity vanishes at the nozzle-to-liquid interface. In fused silica nozzles, negative surface charge will adhere to the walls, while part of the diffuse layer is sheared off. The streaming current I depends on the net ion charge distribution $\rho(r)$ and the velocity profile $u(r)$ of the liquid jet:^{15,16}

$$I = \int_0^{r_n} \rho(r) \cdot u(r) \, dr \quad (4)$$

The bounds of integration are the center of the liquid jet $r = 0$ and the inner radius of the nozzle $r = r_n$. Electrokinetic charging can lead to significant potentials in liquid microjets. Potentials on the order of tens of volts were derived for pure water and alcohols.^{15,16}

We emphasize that the charging of the liquid jet, and thus the streaming current, should be suppressed by a small Debye length, i.e., by high ion concentrations or higher ionic valences (see eq 1). The positive electrokinetic charging in a fused silica nozzle should not depend on the choice of anion, but may slightly depend on the cation—mainly due to size effects.¹³

The electrokinetic charging will be influenced by a change of pH of the solution. Protons can rapidly diffuse into and out of the fused silica glass surface. The fast proton diffusion is followed by a much slower diffusion of larger ions. An equilibrium is reached after several hours. A decrease of the pH will lead to positive charging of the silica surface, and an increase leads to negative charging of the silica surface layer with a potential of up to 59 mV per unit change in pH.¹⁷

When the solution exits the fused silica nozzle and enters the vacuum chamber, the distribution of ions between bulk solution and interface moves toward a new equilibrium. Large and polarizable anions tend to accumulate at the surface.^{18,19} In the case of an iodide solution, we therefore expect an enrichment of iodide at the surface of the liquid jet, while for a fluoride solution we do not expect such an enrichment.

In a recent work, we described time-resolved photoelectron spectroscopy of sodium iodide (NaI) solution for various concentrations of NaI.⁶ In these experiments, photodetachment of iodide led to the creation of solvated electrons and the corresponding photoelectron spectra appeared at different kinetic energies, depending on the salt concentration: for concentrations between 500 and 30 mM, the spectra peaked at

1.35 eV electron kinetic energy (eKE); for 10 mM solution, the peak was at 1.25 eV eKE; for 3 mM solution, the peak was at 0.65 eV eKE. In this work, we relate potential shifts in photoelectron spectroscopy to the charge flow in a liquid jet and investigate the influence of salt concentration on electrokinetic charging.

To relate measured streaming currents to streaming potentials, we assume cylindrical symmetry and solve the Poisson equation $\Delta\Phi = \nabla^2\Phi = -(\rho/\epsilon)$. Assuming cylindrical symmetry is a natural choice, given the cylindrical shape of the liquid jet. However, further assumptions for the boundary conditions are made. The liquid jet in the photoelectron spectroscopy experiment is located approximately in the center between a grounded microskimmer and a grounded magnet, which are about 2 mm apart.⁶ Both microskimmer and magnet have flat faces parallel to the jet propagation direction. The situation is sketched in Figure 2. For the calculations, we

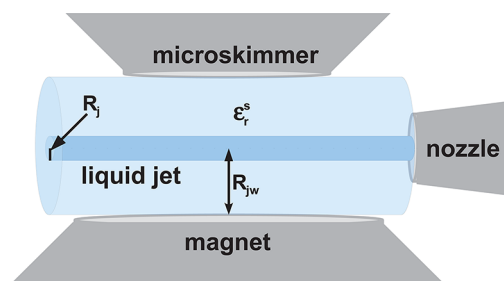


Figure 2. Sketch of the boundary conditions assumed for the modeling of the streaming potential. R_j is the jet radius, R_{jw} the distance between jet and wall, and ϵ_r is the relative permittivity of the jet environment.

replace this complex geometry with an assumed concentric grounded wall at a distance $R_{jw} = 1$ mm from the liquid jet. We also assume that all excess charges are confined within the liquid jet.

The resulting streaming potential is given by

$$\Phi = -\frac{1}{2\pi\epsilon_0\epsilon_r} \frac{I}{v_j} \ln\left(\frac{R_j}{R_{jw}}\right) \quad (5)$$

where ϵ_0 is the vacuum permittivity, ϵ_r is the relative permittivity of the surrounding of the liquid jet, I is a measured

current, v_j is the flow velocity of the liquid jet, and R_j is the radius of the jet in the vacuum chamber. We want to stress that eq 5 differs in R_{jw} from the equations given in refs 15 and 16. Faubel et al. and Holstein et al. arbitrarily set the boundary condition $\Phi = 0$ at $R_{jw} = 1$ m. For the same streaming current, the derived streaming potentials will differ significantly when a more reasonable value for R_{jw} is chosen. If a streaming current of 10 nA is measured for a liquid jet with diameter of $6.55 \mu\text{m}$, the formula used in refs 15 and 16 derives a streaming potential of 18 V, while the boundary conditions considered here ($R_{jw} = 1$ mm) will yield 8 V.

EXPERIMENTAL SETUP

We employ the liquid microjet technique described by Faubel et al.²⁰ The streaming current in the liquid jet was determined as described by Holstein et al.;¹⁶ i.e., we measured an electric current between a beam catcher (a folded copper plate) and the grounded experimental chamber. Our experimental setup is shown in Figure 3.

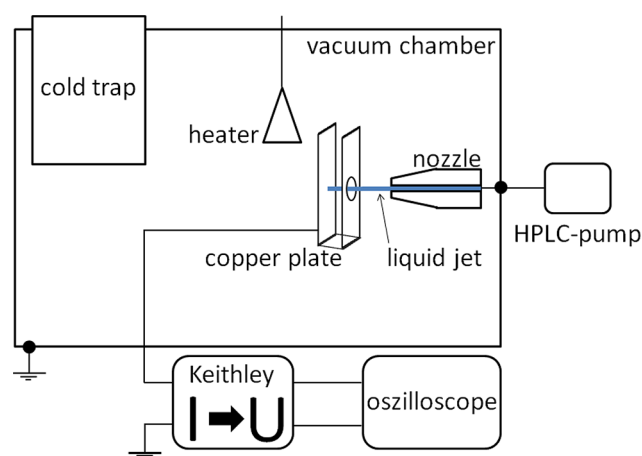


Figure 3. Sketch of the experimental setup: an HPLC pump pressed the sample solution through a fused silica nozzle and produced a liquid microjet. The liquid jet hit a folded copper plate, which was heated by a 50 W halogen bulb. A Keithley current-to-voltage converter measured the current between the copper plate and the grounded wall.

A high-pressure liquid chromatography pump (HPLC pump) pushed the sample solution through a fused silica nozzle with an inner diameter of $15 \mu\text{m}$ and a length of 30 mm into the vacuum chamber. The flow of the liquid jet within the nozzle and shortly after the nozzle exit was laminar. After a few millimeters (depending on the flow rate), the jet broke apart into small droplets. The flow rate was varied between 0.2 and 0.6 mL/min, which corresponds to velocities of about 20–60 m/s. Due to evaporation, the radius of the liquid jet was smaller than the nozzle orifice. By analyzing the Fraunhofer diffraction pattern in the laminar region of the jet from a $13 \mu\text{m}$ diameter nozzle, we determined the jet diameter in vacuum to be $8 \mu\text{m}$. For the $15 \mu\text{m}$ diameter nozzle used for the present studies, we estimate a jet diameter in vacuum of about $10 \mu\text{m}$. Two cold traps were used to freeze out the water vapor in the vacuum chamber.

About 7 cm downstream from the nozzle exit, the liquid jet hit a copper plate. We used a folded copper assembly as sketched in Figure 3, to avoid charge dissipation by droplets that splash away from the copper plate. To avoid freezing of the jet on the copper plate, we heated the plate with two 50 W

halogen bulbs. Apart from a signal cable leading to a Keithley current-to-voltage converter (model 427), the copper plate was electrically isolated. When the liquid jet was running, we measured currents in the nanoampere range flowing from the copper plate to ground. When the liquid jet was turned off, no current was detected.

The experimental setup for measuring photoelectron spectra used the same liquid jet geometry and is described in detail elsewhere.⁶ Photoelectrons were collimated in a magnetic-bottle time-of-flight spectrometer and photoelectron detection occurred with an efficiency close to unity. We detected photoelectrons in counting mode and worked with low count rates on the order of 10 electrons per pulse, hence we can exclude any space charge or plasma effects.

RESULTS AND DISCUSSION

In Figure 4, we show the measured streaming currents for aqueous sodium iodide (NaI, 1–500 mM), aqueous potassium

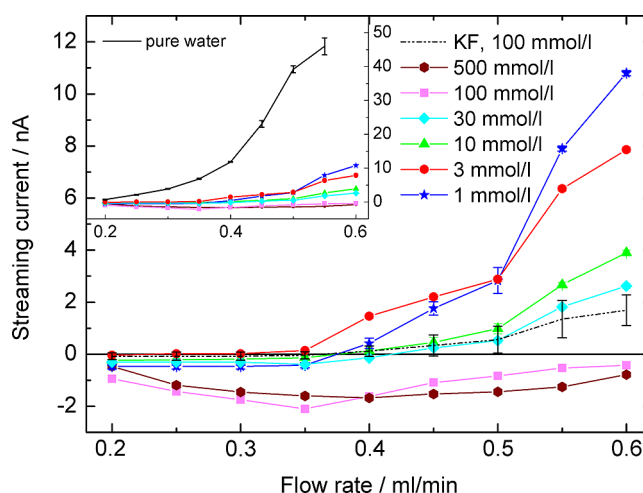


Figure 4. Measured streaming current as a function of the liquid jet flow rate for aqueous sodium iodide (colored traces), potassium fluoride (dash-dotted black trace), and distilled water (black trace in inset). Error bars represent the standard deviation for each point.

fluoride (KF, 100 mM), and pure water as function of the liquid jet flow rate.

The streaming currents of aqueous NaI are negative at low flow rates but increase with the flow rate. For low ion concentrations and large flow rates, the currents become positive. The streaming currents at high concentrations (100 and 500 mM) are negative at all flow rates and show a minimum at a flow rate of about 0.4 mL/min. At the highest flow rate considered here (0.6 mL/min), the streaming currents are inversely correlated with the concentration. The latter observation nicely agrees with our expectations based on the inverse correlation between ion concentration and the size of the diffuse ion layer as discussed in the Introduction. The streaming current for a pure water jet is significantly larger than that of all salt solutions. At a flow rate of 0.5 mL/min, the current for pure water is 40 nA, 15 times larger than that for the 3 mM NaI solution.

The streaming currents for a 100 mM KF solution are positive for all flow rates and increase monotonously. The currents remain almost negligible up to a flow rate of 0.4 mL/min. At flow rates greater than 0.4 mL/min, the data show a trend which is parallel to that for the 100 mM NaI solution.

This is consistent with a similar Debye screening of the negative surface charge for the case of NaI and KF solutions.

The experimentally observed inversion of the current as a function of the flow rate for NaI cannot be explained with a simple dipolar interface layer, as depicted in Figure 1. Instead, a multipolar charge distribution as shown in Figure 5 must be

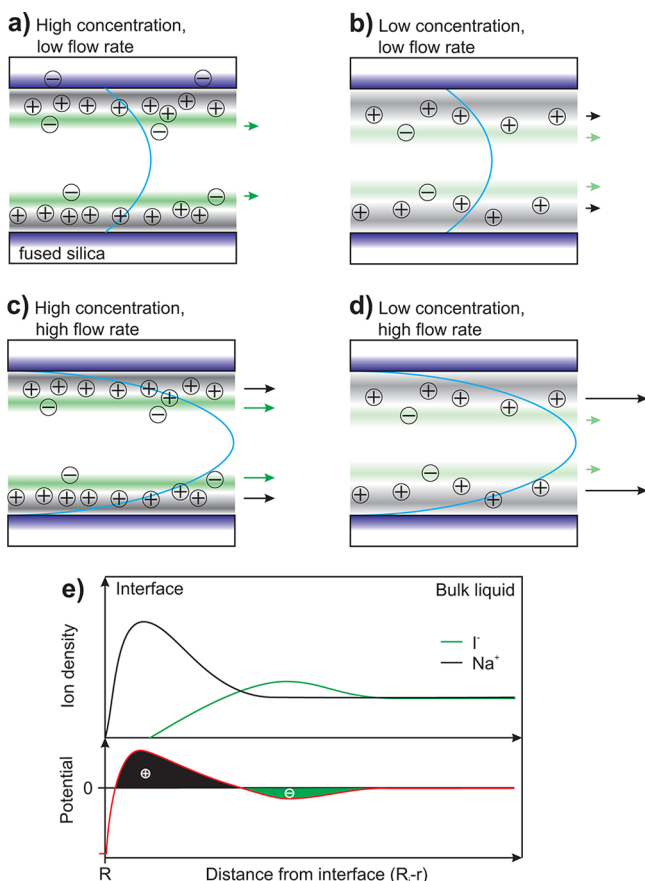


Figure 5. Schematic depiction of the radial charge distribution of iodide anions (green) and sodium cations (gray) within the fused silica nozzle. The fused silica nozzle surface is negatively charged. Sodium counterions form a diffuse Gouy–Chapman layer. To explain our data, we postulate an additional negatively charged layer of iodide ions extending beyond the Gouy–Chapman layer. At high ion concentrations (a,c), the size of the diffuse layer is small. For low flow rates (a), the velocity gradient near the wall is small and a significant negative current is caused by predominant transport of negative ions farthest from the interface. At higher flow rates, the velocity gradient near the wall increases and increasing cationic charge transport leads to a suppression of the negative current. At low ion concentrations (b,d), the size of the cationic diffuse layer is larger, and hence more cations are carried away and dominate the charge transport. At large flow rates (d), the diffuse cationic layer is sheared off and causes significant positive currents.

postulated to explain our experimental results. The proposed charge distribution contains two nodes of changing polarity and therefore resembles the predicted charge distribution in MD simulations for concentrated aqueous NaI solution or even pure water at the water–air interface^{2,21} (Figure 5e). As compared to the purely electrostatic Debye model, the charge distribution contains an additional anionic layer at distances beyond the diffuse cationic Gouy–Chapman layer. Specific interactions and solvation effects, both of which are not part of the Debye model, may play a significant role in concentrated solutions

with small Debye radii and cause a multipolar charge distribution in the vicinity of the interface.

Figure 5a–d illustrates the effect of a multipolar charge distribution for four different scenarios involving varying ion concentrations and flow rates. For large ion concentrations and small flow rates (Figure 5a), the Debye length for the cationic diffuse layer is small and charge separation due to shearing off positive charges is negligible. For increasing but small flow rates, we therefore observe negative currents due to the predominant transport of anions from the innermost, negatively charged layer. In this regime, we observe a linear increase of the negative current with the flow rate ($I = dQ/dt = (Q/L)v_i$). For large flow rates, the velocity gradient across the diffuse cationic layer becomes steeper and more cations are swept away, which leads to a reduction of the negative currents (Figure 5c).

At small ion concentrations (Figure 5, b and d), the Debye length is larger, and so is the extent of the diffuse ion layer. As a result, the velocity gradient across the diffuse layer is sufficient to carry away cations and the currents observed for dilute solutions in Figure 4 therefore increase monotonously and increase most dramatically for the more dilute solutions.

The surface charge of silica is largely governed by the cations, and aqueous KF and NaI solutions induce similar surface charges at neutral pH.¹³ Solutions with identical concentration also have the same Debye length (see eq 1) and we expect a similar charge distribution at the nozzle interface. However, the fluoride anion is significantly smaller than the iodide anion. Hence, the specific ion interactions and related deviations from the Debye–Hückel theory are expected to be different. We observe no negative currents for KF solution (Figure 4). This can be explained by a less pronounced or absent second anionic layer for aqueous KF (Figure 6).

The measured streaming currents are directly related to a potential difference between the surface of the liquid jet and the grounded wall, which can be calculated with eq 5. In photoelectron spectra, this potential difference will shift all observed photoelectron bands. In Figure 7a), we show corresponding shifts in photoelectron spectra of the solvated electron,^{6,10} measured for multiple NaI salt concentrations at a flow rate of 0.5 mL/min. The comparison of potential shifts in photoelectron spectra with those calculated from streaming currents (Figure 7b) reveals a surprising difference between the two: the observed potentials in photoelectron spectra are much lower than those expected from the streaming currents.

The jet potential calculated from streaming currents strongly decreases with increasing salt concentration. Significant positive potentials are calculated for small ion concentrations and correspond to the positive streaming currents shown in Figure 4. At concentrations between 30 and 100 mM, the potential changes sign to negative values.

The jet potentials observed in time-resolved photoelectron spectra at low electron kinetic energies ($eKE < 5$ eV)^{5,7,10} (Figure 7, a and b) are small and decrease with increasing ion concentration. Binding energies of the solvated electron measured in different groups and under different experimental conditions agree very well and can therefore be considered as reliable, despite the novelty of the experimental technique. The discrepancies between potentials observed in photoelectron studies and those derived from electrokinetic current measurements force us to revisit eq 5, which clearly fails to describe the jet potential. Equation 5 was derived under the assumption that all charges are located within the jet. In the following, we show that this is not necessarily the case.

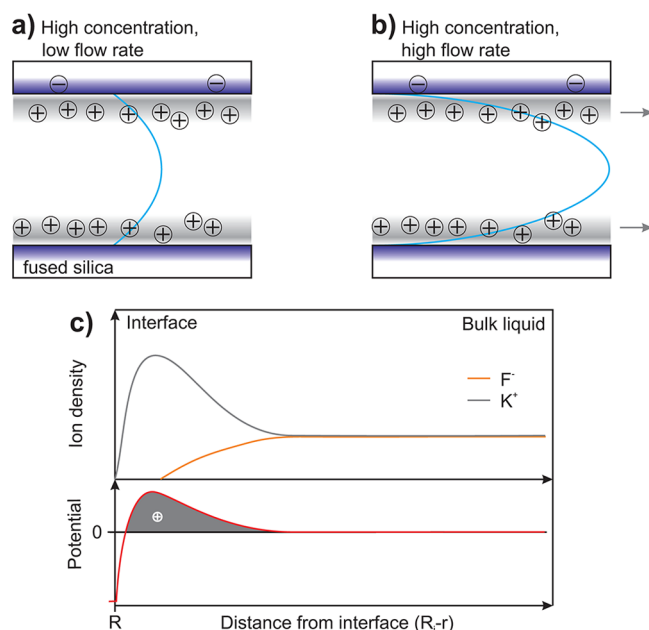


Figure 6. Schematic depiction of the radial charge distribution of fluoride anions (orange) and potassium cations (gray) within the fused silica nozzle. The negatively charged silica surface attracts potassium cations, which form a diffuse Gouy–Chapman layer. Due to the high (100 mM) ion concentration, the diffuse layer is small and at low flow rates (a), charge separation is small. At larger flow rates (b), the increased velocity gradient near the surface causes increasing cationic currents.

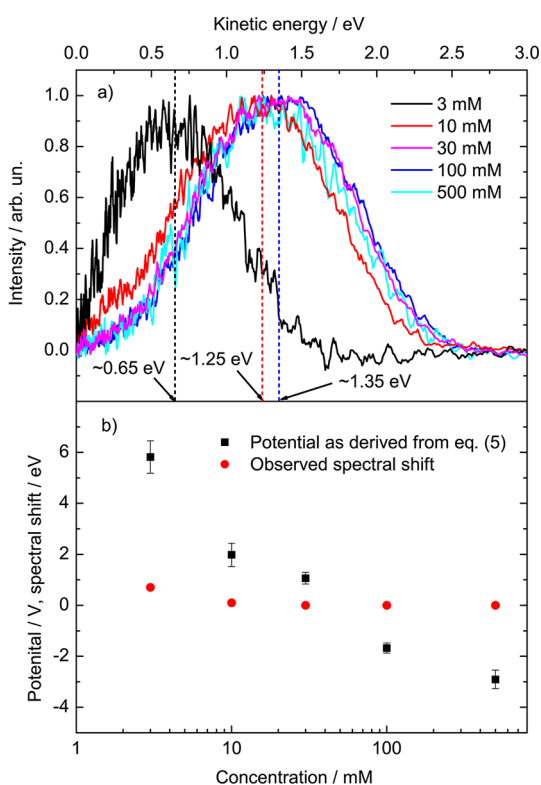


Figure 7. (a) Normalized photoelectron spectrum of the solvated electron in aqueous NaI solution of different salt concentrations. (b) Jet potential calculated with eq 5 from measured streaming currents and the observed potential shift in photoelectron spectra as a function of the salt concentration with a flow rate of 0.5 mL/min.

In Figure 8, we show time-resolved photoelectron spectra for a liquid jet of 100 mM NaI solution (Figure 8b,c) and the vapor

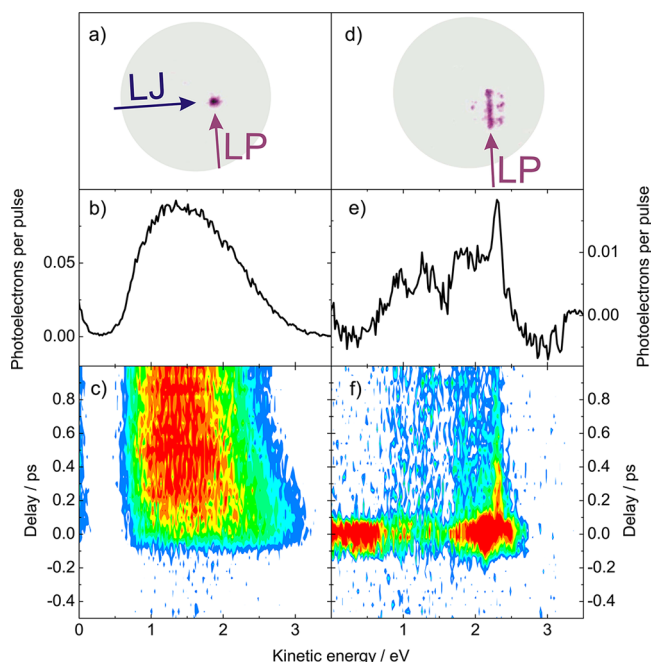


Figure 8. Photoelectron signal from a liquid jet (LJ) of an 100 mM aqueous NaI solution (a–c) and from the gas phase around the liquid jet (d–f). (a) The photoelectron image at the detector reveals the tight localization of the electron source when the signal emanates from the liquid jet. Signals from the surrounding gas phase are negligible. (b) Integrated electron spectra for delays > 0.2 ps and (c) time-resolved spectra are unstructured, due to inhomogeneous broadening in the jet. (d) The vapor phase surrounding a dislocated jet is ionized along the laser propagation direction (LP) and (e,f) reveals structured electron spectra. Signals due to one-color multiphoton ionization have been subtracted.

phase around the liquid jet (Figure 8e,f). The magnetic bottle produces an enlarged image of the electron source on the detector (multichannel plate coupled to a phosphor screen). In Figure 8a,d, we show the detector images for the interaction of the laser pulses with the liquid jet and with the vapor phase surrounding the jet.

If the laser interacts with the liquid jet, the size of the electron source is limited by the diameter of the liquid jet and the focal spot size of the laser pulse (Figure 8a) and we observe a very localized electron source. Only vapor is ionized if the liquid jet is displaced and the photoelectron signals decrease by orders of magnitude, mainly due to the reduced particle density. To compensate for the signal loss, the laser pulse energy was increased to $\sim 1\text{--}10\ \mu\text{J}$ each for pump and probe pulses (laser intensity up to $\sim 10^{12}\ \text{W}/\text{cm}^2$), as compared to a few 10s of nanojoules in the case of the liquid jet experiment (laser intensity up to $\sim 10^9\ \text{W}/\text{cm}^2$). The shape of the electron source is also significantly altered to an electron line source: the laser pulse ionizes molecules along its propagation direction (Figure 8d). Signals from the liquid and from the gas phase are therefore easily distinguished and can be interpreted independently.

The time-dependent photoelectron spectrum of the NaI solution (Figure 8c) is governed by the generation of a solvated electron by the 5.2 eV pump pulse.¹⁰ The corresponding charge-transfer-to-solvent state is the only excited state

accessible and we can assign all observed signals to the solvated electron.

The signal for the vapor phase is significantly different and consists of several structured features. A strong signal close to the temporal overlap is assigned to cross-correlation signal. Some photoelectron signal persists for delays significantly exceeding the cross-correlation width of ~ 100 fs, but appears only if the 5.2 eV pulses come first. This pump–probe signal must stem from an excited species.

Gas-phase water and water clusters in the vapor phase surrounding the liquid jet have no accessible excited states in the spectral regime of the pump photon.²² We propose that the vapor phase contains $\text{I}^-(\text{H}_2\text{O})_n$ water clusters and that the observed signal is due to solvated electrons formed by photodetachment of iodide in these clusters. The sharp features in the vapor-phase photoelectron spectra (cf. Figure 8b) may correspond to signal from different cluster sizes. The postulation of charge evaporation should not be surprising: when the liquid jet enters vacuum, water strongly evaporates from the liquid surface. The evaporation rate is on the order of $\sim 3 \mu\text{m/s}$,²³ and of similar magnitude as the diffusion velocity of halide anions in water. Iodide accumulates at the liquid surface, but we would even expect the appearance of less surface active ions in the gas phase. Please note that, just after entering the vacuum, the liquid to vacuum interface is far from thermal equilibrium and that the solvation energy for an halide located in a water cluster or in bulk water is very similar, which makes the evaporation of clusters containing ions energetically possible.

The charged ion–water clusters around the water jet will contribute to measured currents, but require a modified charge distribution model: the net excess charge is no longer exclusively located within the jet as assumed in eq 5, but at a larger distance from the jet axis. This significantly reduces the potential difference between the jet surface and the skimmer and may thus explain the observed discrepancy between the estimated potential difference from eq 5 and the potentials observed in photoelectron studies.

Summarizing, we have shown that electrokinetic charging is suppressed by addition of salts in the millimolar concentration regime. We observed similar charge suppression by NaI and KF salt solution and, based on the qualitative consideration of Debye radii, we would not expect significantly different behavior for other alkali halide solutions at neutral pH. For NaI at large ion concentrations, the electrokinetic current varies nonmonotonously with the jet velocity, which can be explained by a multipolar charge distribution at the interface within the nozzle. Based on the assumption that all excess charges are located within the liquid jet, the calculated potential difference between the surface of the jet and the skimmer is on the order of several volts, even for large salt concentrations. This contradicts results from liquid jet photoelectron spectroscopy at low kinetic energies and we conclude that a significant amount of excess charge is not confined within the jet, but is evaporated. Indeed, photoelectron spectra indicate that charged clusters are found in the vapor phase around the liquid jet. A correspondingly modified model with an extended charge distribution can explain the reduced potential differences between liquid jet and spectrometer skimmer, which are observed in photoelectron spectroscopy. It would be interesting to use mass spectrometry techniques as LILBID²⁴ to search for these charged clusters around liquid jets in vacuum.

Our findings show that the analysis of liquid jet photoelectron spectra requires the careful assessment of electrokinetic charging effects. At low photon energies, a suitable in situ calibration has not been described, and hence the charging effects must be considered systematically. At larger photon energies, photoelectron spectra of the liquid jet and the vapor phase can be recorded simultaneously and narrow gas-phase lines can be used for calibration. As long as such a possibility is not available at low photon energies, a salt concentration dependence should be measured and the studies of interest should be performed in a region of negligible concentration dependence. For aqueous solution, our results show that addition of at least 10–30 mM salt is required to suppress the electrokinetic charging efficiently.

AUTHOR INFORMATION

Corresponding Author

*E-mail: luebecke@mbi-berlin.de.

Notes

The authors declare no competing financial interest.

ACKNOWLEDGMENTS

The authors thank F. Noack for his support by providing the laser system in the femtosecond application laboratory of the Max-Born-Institut Berlin. This work was financially supported by Deutsche Forschungsgemeinschaft, Project LU 1638/1-1.

REFERENCES

- (1) Winter, B.; Weber, R.; Schmidt, P. M.; Hertel, I. V.; Faubel, M.; Vrbka, L.; Jungwirth, P. *J. Phys. Chem. B* **2004**, *108*, 14558–14564.
- (2) Ottosson, N.; Heyda, J.; Wernersson, E.; Pokapanich, W.; Svensson, S.; Winter, B.; Öhrwall, G.; Jungwirth, P.; Björneholm, O. *Phys. Chem. Chem. Phys.* **2010**, *12*, 10693–10700.
- (3) Brown, M.; Winter, B.; Faubel, M.; Hemminger, J. C. *J. Am. Chem. Soc.* **2009**, *131*, 8354–8355.
- (4) Buchner, F.; Schultz, T.; Lübcke, A. *Phys. Chem. Chem. Phys.* **2012**, *14*, S837–S842.
- (5) Tang, Y.; Suzuki, Y.-I.; Shen, H.; Sekiguchi, K.; Kurahashi, N.; Nishizawa, K.; Zuo, P.; Suzuki, T. *Chem. Phys. Lett.* **2010**, *494*, 111–116.
- (6) Buchner, F.; Lübcke, A.; Heine, N.; Schultz, T. *Rev. Sci. Instrum.* **2010**, *81*, 113107.
- (7) Shreve, A. T.; Yen, T. Y.; Neumark, D. M. *Chem. Phys. Lett.* **2010**, *493*, 216–219.
- (8) Siefermann, K. R.; Liu, Y.; Lugovoy, E.; Link, O.; Faubel, M.; Buck, U.; Winter, B.; Abel, B. *Nat. Chem.* **2010**, *2*, 274–279.
- (9) Winter, B.; Weber, R.; Widdra, W.; Dittmar, M.; Faubel, M.; Hertel, I. V. *J. Phys. Chem. A* **2004**, *108*, 2625–2632.
- (10) Lübcke, A.; Buchner, F.; Heine, N.; Hertel, I. V.; Schultz, T. *Phys. Chem. Chem. Phys.* **2010**, *12*, 14629–14634.
- (11) Ong, S.; Zhao, X.; Eienthal, K. B. *Chem. Phys. Lett.* **1992**, *191*, 327–335.
- (12) O'Reilly, J. P.; Butts, C. P.; I'Anson, I. A.; Shaw, A. M. *J. Am. Chem. Soc.* **2005**, *127*, 1632–1633.
- (13) Dove, P. M.; Craven, C. M. *Geochim. Cosmochim. Acta* **2005**, *69*, 4963–4970.
- (14) Hamann, C. H.; Vielstich, W. *Electrochemistry*; Wiley-VCH: Weinheim, Germany, 1998.
- (15) Faubel, M.; Steiner, B. *Ber. Bunsenges. Phys. Chem.* **1992**, *96*, 1167–1172.
- (16) Holstein, W. L.; Hayes, L. J.; Robinson, E. M. C.; Laurence, G. S.; Buntine, M. A. *J. Phys. Chem. B* **1999**, *103*, 3035–3042.
- (17) Haber, F.; Klemensiewicz, Z. *Z. Phys. Chem.* **1909**, *67*, 385–431.
- (18) Jungwirth, P.; Tobias, D. J. *Chem. Rev.* **2006**, *106*, 1259–1281.
- (19) Petersen, P. B.; Johnson, J. C.; Knutsen, K. P.; Saykally, R. J. *Chem. Phys. Lett.* **2004**, *397*, 46–50.

- (20) Faubel, M.; Steiner, B.; Toennies, J. P. *J. Chem. Phys.* **1997**, *106*, 9013–9031.
- (21) Vácha, R.; Rick, S. W.; Jungwirth, P.; de Beer, A. G. F.; de Aguiar, H. B.; Samson, J.-S.; Roke, S. *J. Am. Chem. Soc.* **2011**, *133*, 10204–10210.
- (22) Mota, R.; Parafita, R.; Giuliani, A.; Hubin-Franskin, M. J.; Lourenco, J. M. C.; Garcia, G.; Hoffmann, S. V.; Mason, N. J.; Ribeiro, P. A.; et al. *Chem. Phys. Lett.* **2005**, *416*, 152–159.
- (23) Faubel, M.; Schlemmer, S.; Toennies, J. P. *Z. Phys. D: At., Mol. Clusters* **1988**, 269–277.
- (24) Kleinekofort, W.; Avdiev, J.; Brutschy, B. *Int. J. Mass Spectrom. Ion Processes* **1996**, *152*, 135–142.